Journal of Forestry Research (2025) 36:81
https://doi.org/10.1007/s11676-025-01870-7

ORIGINAL PAPER

Mapping discrete forest age classes of Mediterranean pinelands since the pre-satellite era using historical orthoimage mosaics and machine learning

Vicent A. Ribas-Costa[1] · **Andrew Trlica**[2] · **Aitor Gastón**[1]

Received: 15 July 2024 / Accepted: 1 February 2025 / Published online: 8 June 2025
© The Author(s) 2025

Abstract Land use/land cover (LULC) change monitoring is critical for understanding environmental and socio-economic processes and to identify patterns that may affect current and future land management. Forest cover evolution in the Mediterranean region has been studied to better understand forest succession, wildfires potential, and carbon stock assessment for climate change mitigation, among other reasons. However, though multiple sources of current LULC exist, data from last century's forest cover are less common, and are normally still reliant on locally orthophoto-interpreted data, making continuous maps of historical forest cover relatively uncommon. In this work, a pipeline based on image segmentation and random forest LULC modeling was developed to process three high resolution orthophotos (1956, 1989, and 2021) into LULC continuous land cover maps of Spain's island of Ibiza. Next, they were combined to quantify forest evolution of Mediterranean Aleppo pine (*Pinus halepensis* Mill.) and to generate a continuous map of forest age classes. Our models were able to differentiate forestland with an accuracy higher than 80% in all cases, and were able to approximate forestland cover change since the mid-twentieth century, estimating 21,165 ± 252 ha (37.0 ± 0.4%) in 1956, 27,099 ± 472 ha (46.8 ± 0.8%) in 1989, and 30,195 ± 302 ha (52.8 ± 0.5%) in 2021, with a mean increase of 139 ± 6 ha (0.46 ± 0.02%, calculated from current forest cover estimate) per year. The most important variables for the identification of the forestland were the terrain slope and the image gray level or color information in all orthophotos. When combining the information from the three periods, the analysis of forest evolution revealed that a significant portion of current forest cover, approximately 15,776 ha, fell within the 75–120 year age range, while 5388 ha fell within the range of 42–74 years, and 9022 ha within the 10–41 years forest age class. Younger forests, except when mapped after known wildfires, were not considered due to the limitations of the methodology. When compared to forest age data based on ground measurements, significant differences were found among each of the remotely sensed forest age classes, with a mean difference of 13 years between the theoretical age class central value and the real observed plot average age. Overall, 63% of the forest inventory plots were assigned with the correct forest age class. This work will allow a better understanding of long-term Mediterranean forest dynamics and will help landowners and policymakers to better respond to new landscape planning challenges and achieve sustainable development goals.

Keywords Aerial orthophotos · Image segmentation · Random forest · Landscape evolution · Forest age

Project funding: This study was supported by the Doctoral INPhINIT Retaining Fellowship (LCF/BQ/DR22/11950023) from la Caixa Foundation (ID 100010434, Barcelona, Spain), with additional funding through grant PID2021 127241OB I00 from the Spanish Ministry of Science and Innovation/Agen- cia Estatal de Investigación (MCIN/AEI/10.13039/501100011033), co funded by the European Regional Development Fund (ERDF) under the A Way of Making Europe.

The online version is available at http://link.springer.com.

Corresponding editor: Tao Xu.

✉ Vicent A. Ribas-Costa
va.ribas@upm.es; vicentribas11@gmail.com

[1] ETSI Montes, Forestal y del Medio Natural, Centro Para La Conservación de La Biodiversidad y El Desarrollo Sostenible (CBDS), Universidad Politécnica de Madrid, Calle José Antonio Novais 10, 28040 Madrid, Spain

[2] Department of Forestry and Environmental Resources, NC State University, Raleigh, NC 27695, USA

Introduction

Mapping and monitoring Earth's surface cover is of utmost importance for understanding the multiple environmental and socioeconomic changes that affect urban planning, environmental management, or regional administration (Patino and Duque 2013; Liu et al. 2017; Zhang et al. 2019). The Earth's surface cover is normally referred to as land use/land cover (LULC) when describing landscape at the human scale, as it can help to identify ecosystem vulnerabilities, environmental trends, and human-related processes (Bey et al. 2016; Gómez et al. 2016; Guzha et al. 2018). Land cover relates to natural or semi-natural lands characterized by biophysical cover of the Earth's terrestrial surface, whereas land use is the result of human activities that modify the landscape (Bakker and Veldkamp 2008; Souza et al. 2020). Evaluating both historical and current LULC conditions that arise from natural and anthropogenic drivers is indispensable for generating accurate forecasts concerning future LULC dynamics. These LULC dynamics are also referred to as land-use/land-cover changes (LULCC) and are crucial to understand trends in landscape evolution, from both ecological and socioeconomic perspectives (Bakker and Veldkamp 2008; Di Fazio et al. 2011; Gómez et al. 2016). Particularly in the Mediterranean Basin, one of the most studied dynamics is historic human population relocation, which resulted in agricultural land abandonment and forest re-colonization since the early twentieth century (Collantes 2007; Di Fazio et al. 2011; Bajocco et al. 2012; Vidal-Macua et al. 2018; Delgado-Artés et al. 2022). Population movement and densification of coastal margins along the Balearic Archipelago happened at a different rate and followed different patterns than along other European coasts (Pons and Rullan 2014a, 2014b; Ramón-Cardona and Serra-Cantallops 2014), which also resulted in different LULC changes within the interior of the islands.

Remote sensing has been a key tool for mapping Land LULC since the early twentieth century, with long-term and historical aerial and satellite observations making it possible to monitor and capture changes over time. The first expression of remotely sensed LULC assessment is found in historical aerial photographs (HAPs) (Pinto et al. 2019). Multiple HAPs can be stitched to produce a continuous orthorectified image (orthophoto) of an area of interest, which can be used for historic landscape assessment and monitoring (Grottoli et al. 2021; Heisig and Simmen 2021; Van den Broeck et al. 2022; Morford et al. 2024). In Spain, although earlier aerial photos were acquired, it was not until after World War II that an agreement between the American Army Map Service and the Spanish Ministry of Defense permitted the acquisition of two nation-wide aerial surveys: one in 1945–1946 (American Flight Series A) and one in 1956–1957 (American Flight Series B) (Fernández García 2015). Later, an aerial acquisition completed only by Spanish personnel (the so-called National Flight Series C) took place in 1967–1968. Of these three acquisitions of HAP, the American Flight Series B is the most used for long-term landscape analysis due to its higher quality, and complete coverage of the country, as well as its public availability as a panchromatic digital orthophoto after the scanning of the original prints.

Multispectral satellite imagery is one of the most commonly used techniques for LULC mapping, often relying on pixel-based land classification algorithms (Sharma et al. 2018; Zhang et al. 2019; Langenkamp and Rienow 2023). There is, however, another technique increasingly used in both multispectral and low-spectral optical data, such as the previously mentioned panchromatic (or even RGB) orthophotos (Maxwell et al. 2019; Atik and Ipbuker 2021; Van den Broeck et al. 2022) known as Geographic object-based image analysis (GEOBIA). While pixel-based methods rely only on the spectral reflectance signature to assign a LULC class to each pixel, without considering neighboring pixels (Zhang et al. 2019), the GEOBIA workflow performs a first segmentation of the image based on the similarities between pixels, after which zonal statistics of spectral properties and potentially ancillary non-image data is appended to each of the objects generated (Castilla and Hay 2008; Blaschke 2010). The actual assignment of a LULC class to either the pixel or the object is normally performed with a statistical technique, such as random forest (RF), support vector machine (SVM), K-nearest neighbor (KNN), or even logistic regressions (LR) (Das and Pandey 2019; Maxwell et al. 2019; Chmielewski et al. 2020; Atik and Ipbuker 2021). The GEOBIA method, therefore, is much more useful for orthophotos with low spectral information, such as panchromatic images derived from HAP. Additionally, it is also claimed that a pixel by itself does not represent any geographical feature such as a forest stand, whereas the GEOBIA approach enhances stand-level research (Varo-Martínez et al. 2017; Bey et al. 2016) in forestry applications. Deep learning is increasingly being used to map LULC and specifically forest cover and properties from remote sensing products, and can be applied at the pixel level for very high spatial resolution (Nguyen et al. 2022; Tolan et al. 2024).

When these methodologies are applied to a specific time series of data, the characterization of LULCC within a specific time interval improves the understanding of environmentally or human driven processes. Focusing on forested areas, characterizing disturbances, management, or evolution trends are some of the most common uses of time-wise LULCC monitoring (Kennedy et al. 2010; Wężyk et al. 2018; Thomas et al. 2021). Specifically, a major objective of forest assessment over time is to obtain and map stand age across the landscape. Forest age (or stand-replacing disturbances) is an important stand

attribute, exerting a pivotal influence on carbon dynamics within forest ecosystems (Oliver and Larson 1996; Véga and St-Onge 2009; Yang et al. 2020), and therefore closely related to several forest productivity estimates. However, traditional dendrochronological approaches are expensive and labor- and time-inefficient (Speer 2010; Liu et al. 2018), as well as spatially discrete and therefore difficult to use to interpolate over large areas. Alternatively, different remotely sensed methods exist to obtain an accurate and spatially explicit estimate of forest evolution/age, mainly based on the following approaches (Maltman et al. 2023): (1) the use of single or multiple measurements of tree-heights and inverted allometric equations (Véga and St-Onge 2009; Frate et al. 2016; Yang et al. 2020); (2) analyzing the reflectance of multispectral or hyperspectral optical data (Buddenbaum et al. 2005; Chen et al. 2018); (3) the use of aerial photos time series (Wężyk et al. 2018; Morford et al. 2024; Nguyen et al. 2024).

Multispectral methodologies, while very appealing due to higher time resolution, are restricted to the existent optical satellite record, starting at the earliest in 1972 when Landsat-1 was launched with its 60-m resolution Multi-Spectral Scanner (MSS) (Belward and Skøien 2015). However, in many parts of the world these satellite records were fractional until the arrival of Landsat-7 in 1999 (Wulder et al. 2016). As a result, globally comprehensive satellite data availability covers only 50 years at the most, which is a limiting factor for mapping longer natural or anthropic change processes (Kaim et al. 2016; Fu et al. 2017; Delgado-Artés et al. 2022). With this context, HAP provide a critical source of information as it allows users to visualize cover change patterns that need a larger time span to evolve, unfolded at resolutions aligned with modern aerial and satellite mapping technologies. Specifically, the combined use of historic and modern orthophotography allows for a long-term analysis to study forest evolution or age classification (Ameztegui et al. 2021; Morford et al. 2024; Nguyen et al. 2024). Nonetheless, there is a notable lack of published research that continuously monitors forests using multi-sensor historical time series with more than two data acquisitions (Nguyen et al. 2024).

In this context, the specific objectives of this study were:

1. Generate interpretable LULC classification models for three periods of the island of Ibiza (1956, 1989, and 2021) covering over 65 years of land use/land cover changes and territorial development..
2. Develop and validate a methodology for forest age classification of naturally regenerated pine forests.
3. Visualize the spatial patterns of *Pinus halepensis* Mill. forest expansion in the past 65 years.

Materials and methods

Overview

The next section outlines the data and methods utilized in this study. Figure 1 presents a workflow diagram illustrating the various steps taken to achieve the final results.

Aerial orthorectified photographs

Three orthophotos (two HAP-based, one modern) were used in this research. The first collection (American Flight Series B) was acquired in July 1956; the second collection, the Cartography and Geography Institute of the Balearic Islands 1989–1990 flight; and the third, the Spanish National Program for Aerial Orthophoto flight of June 2021 (Table 1). The total time span was of 65 years, with approximately 33-year intervals among aerial photos.

Image segmentation

Following a similar approach as in previous studies (Tassi and Vizzari 2020), an unsupervised segmentation of each of the aerial images as a part of our GEOBIA workflow was performed. Prior to segmentation, image smoothing and preprocessing was performed, including down-sampling of the original images to a resolution of 2.5 m, since broader resolutions allow a better segmentation at the landscape scale (Maxwell et al. 2019; Van den Broeck et al. 2022) while helping reduce the internal variability of objects segmented from high resolution imaging (Wężyk et al. 2018). It is also known that a raw down-sampling can generate noise that affects segmenting power, and accordingly a median filter was applied to remove salt-and-pepper noise, followed by a Gaussian filter to emphasize the edges of the different land cover classes (Almonacid-Caballer et al. 2017; Kwon et al. 2017; Gromada 2022; Langenkamp and Rienow 2023). With this preprocessing, the level of detail of the images was simplified while enhancing the structural differences among land cover classes, with the goal that further processing required less computation time and was more efficient in the continuous segmentation of large and homogeneous areas.

Unsupervised segmentation was performed using the ERDAS Imagine software (Hexagon Geospatial, Stockholm, Sweden), clustering together groups of pixels semantically and structurally similar into segmented objects. This segmentation did not rely on previous training data, and was based only on the image properties, either grayscale, or RGB. This tool allows the user to fine-tune parameters to adjust the resulting segmented image and control the segmented objects' size, shape, and boundaries (Ez-zahouani et al. 2023). This fine-tuning of the segmenting algorithm

can be used to optimize the results of the segmentation process and adapt it to the input data and segmentation objectives. In our case, the segmentation parameters were manually and specifically fine-tuned for each aerial photo (Table 2) and performed a quality control of the generated objects by visually exploring the resulting segmentation after each trial and across the whole study area, especially considering the average object size as an indicator of the segmentation scale (Lu et al. 2021). This fine-tuning was based on the landscape-scale LULC classes that were

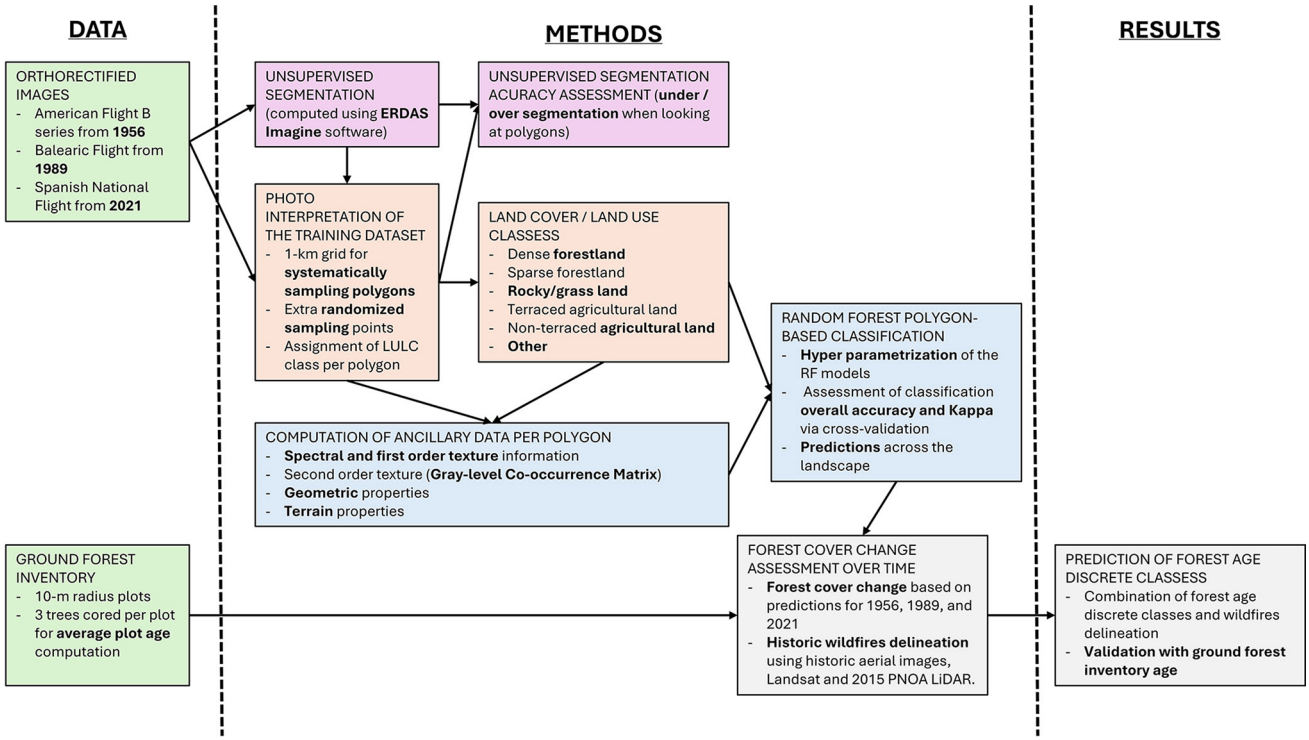


Fig. 1 General overview of the data sources and methodological steps presented in this work. Green indicates data sources; pink indicates segmentation steps; orange indicates LULC-related steps; blue indicates modeling steps; and gray indicates final discrete forest age classification

Table 1 Specific characteristics of the three sets of aerial images

Year	Source	Scale	GSD (m)	Nature
1956	American Map Service and Spanish Air Force (CECAF)	1:33,000	0.5	Analogic, grayscale
1989–1990	Cartography and Geography Institute of the Balearic Islands	1:22,000	0.5	Analogic, grayscale
2021	Spanish National Program for Aerial Orthophoto	1:15,000	0.25	Digital, RGB

GSD: Ground sampling distance

Table 2 Specifications of the preprocessing and segmentation parameters used with each orthophoto

Year	Image preprocessing		Image segmentation				
	Median window size (pixels)	Gaussian kernel radius (m)	Threshold for edge pixel (intensity)	Minimal length of object (pixels)	Minimal value difference (intensity)	Variance factor (intensity)	Minimum size of object (pixels)
1956	3	0.5	22	20	20	10	80
1989	4	0.5	25	20	20	10	80
2021	4	0.5	25	20	20	10	80

Segmentation was performed at a 2.5-m pixel resolution

targeted to be discriminated, as previous research suggests that in image segmentation the scale parameter has a large impact on classification accuracy (Liu and Xia 2010; Smith 2010; Lu et al. 2021). In our methodology, this parameter was affected by all the fine-tuned parameters in the image segmentation section of Table 2, but especially by the variance factor (which controls the intensity variability within a single object) and the minimal length and size of objects (which affects the size and location of small objects). This optimization was based on analyst best-judgement, aiming for a compromise between over-segmentation (e.g., individual trees segmented out of the agricultural land matrix or small forest gaps segmented out of the continuous cover forest), and under-segmentation (e.g., objects including multiple land classes, such as shadowed crops embedded in the same polygon of an adjacent forest patch). A minimum size of object was selected in order to remove noise from the segmented image as in Wężyk et al. (2018), assigning objects below the minimum to a neighboring class.

Land cover and land use classification and modeling

Land cover and land use classes

Multiple proposals for systematic and hierarchical land classification systems exist, with some being accepted throughout Europe for large scale use (Bossard et al. 2000; Büttner et al. 2004). However, classification rules must be adapted to territorial characteristics, data characteristics, and research objectives in order to get more accurate results (Maxwell et al. 2019; Delgado-Artés et al. 2022), especially when the classification is performed after a segmentation procedure (Ez-zahouani et al. 2023).

Though our main objective was to track forest cover changes over time, it was decided to categorize other land cover/uses to (1) get a better understanding of the land change processes that happened in the study area over the study period, and (2) enhance the model's accuracy by maximizing internal homogeneity within land classes while maximizing dissimilarity among them. Field observations and specific knowledge of the study area allowed us to segregate land cover/use into six classes (Table 3): (1) dense forestland (DFL); (2) sparse forestland (SFL); (3) non-forest grassland, scrubland, and sparse rocky areas (RGL); (4) terraced agricultural land (TAL); (5) non-terraced agricultural land (NTAL); and (6) other (OTH). Other studies have used similar classification systems (González-Ávila and Elena-Rosselló 2009; Tadese et al. 2020; Delgado-Artés et al. 2022; Shimizu et al. 2023). We aimed for a simple classification system that could be used for all three orthomosaics (Maxwell et al. 2019), given the panchromatic nature of 1956 and 1989 images and RGB information embedded in the 2021 images.

Training dataset: photo interpretation

Once each of the orthophotos was segmented, the training and validation datasets were built for each orthoimage which consisted of a set of segmented objects converted to digital polygons and manually classified via visual photo interpretation. To do so, a 1-km grid was overlaid over the study area generating 575 points at the intersections of every four cells. These points were then used to select the polygons beneath each of the previous locations for manual photo interpretation and labeling with the correct land cover/use class. With the aim of increasing the total number of training samples, another set of segmented polygons randomly selected throughout the entire dataset was additionally photo interpreted. This randomized mixed sampling method allows the interpreter to assume that each of the classes represented in the study area is represented proportionally in the training and validation dataset, therefore obtaining an unbiased dataset (Stehman 2014) especially in large areas without previous stratification (Ambrosio and Alonso 1993). The final dataset varied in terms of sample size, area, and categories for the three orthoimages (Table 5).

Accompanying the land cover class, each polygon was assigned a series of ancillary input features from the following sources: spectral metrics (gray level or RGB) and first- and second- order texture (or Gray-Level Co-occurrence

Table 3 Mapped classes and descriptions

Class	Code	Description
Dense forestland	DFL	Areas dominated by tall, woody forest vegetation and dense mature forests
Sparse forestland	SFL	Areas dominated by lower size and density of woody forest vegetation (scrub or trees)
Rocky/grass land	RGL	Areas either dominated by low (woody or grassy) vegetation or rocky outcrops with sparse vegetation. This includes, when distinguishable, abandoned agricultural land if not yet colonized by forest
Terraced agricultural land	TAL	Terraced agricultural land, mostly on hillsides
Non-terraced agricultural land	NTAL	Non-terraced agricultural land. This includes the large, flat areas used for wet or dry agriculture or cattle grazing
Other	OTH	All surfaces that do not fall in any of the previous categories: water, impervious surfaces (e.g., roads, airports), urban developed (e.g., pure and mixed developments), beaches or cliffs

Matrix, GLCM) calculated internally from the panchromatic or RGB imagery (the latter after transforming to mean intensity averaging all the bands); geometric properties (i.e., area); terrain-derived properties; and distance to the sea, as we expected this measure to help with the OTH category (Table 4). The terrain-derived properties were derived from the 5-m pixel resolution digital terrain model (DTM) of the Spanish National Orthophotography Plan (PNOA) 2019 LiDAR acquisition, which is available from the Spanish Institute of Cartography and Geography and that was considered stable across the entire time interval. In total, 13 features were used for characterizing objects in the grayscale images and 16 features for the RGB image including three vegetation indices calculated using the color band data.

Following previous studies and the experience of our own data exploration, the final texture variables and the parameters for the GLCM analysis were selected (Maxwell et al. 2019; Tassi and Vizzari 2020; Langenkamp and Rienow 2023). To calculate GLCM features the *ee.Image.glcm* algorithm from the Google Earth Engine platform was used, adopting a kernel size of 2 pixels of the native resolution images given our intention to capture the internal variations of the segmented polygons, such as the agricultural trees in rows in NTAL or the stone walls in TAL. Next, zonal statistics were computed to each raster, summarizing the previous variables per each segment. To do so, the *ee.Reducer* GEE algorithm was used for second-order textural variables and Zonal Statistics in QGIS 3.28.8 (QGIS Development Team 2022) algorithm for the rest of them. For each segmented polygon, the average raster value for each of the metrics considered was obtained.

Training dataset: segmentation accuracy assessment

It is accepted that the generation of a land cover classifier and its accuracy assessment is also a form of segmentation accuracy assessment by itself (Costa et al. 2018). However, as an attempt to better quantify the accuracy of the previous segmentation procedure (Ez-zahouani et al. 2023), during visual evaluation, we determined whether or not each polygon in the training and validation dataset had been over- or under-segmented. The number of polygons that had mixed classes (i.e., had been under-segmented) was then evaluated, and the total amount of mis-segmented area implied was calculated. The size of the dataset (per photo) in absolute and relative terms of polygons and area were reported (Table 5). Given that the quality the reference data has a direct impact on the land cover classification model (Gómez et al. 2016) and must have sufficient accuracy to enable robust validation (Wulder et al. 2006), the training polygons identified to have such problems were manually corrected.

To reduce model uncertainty in minor land classes, the only body of water in the study area was manually segmented, as well as the main urban areas of the island in 1956 and 1989 orthophotos. For the latest image, 2021, the National Geographic Institute (IGN) population database

Table 4 Input features used in the land classifier model

Group	Variable name	Abr	Band/formula/reference used	Layer	GSD (m)
Spectral and First-Order texture	Average	SPECavg	Grayscale/R, G, B	Grayscale/RGB	2.5
	Standard deviation	SPECstd	Grayscale/R, G, B	Grayscale/RGB	2.5
	Normalized Green–Red Difference Index	NGRDIavg	$\frac{G-R}{G+R}$	RGB	2.5
	Visible Band Difference Vegetation Index	VDVIavg	$\frac{2*G-R-B}{2*G+R+B}$	RGB	2.5
	Green Leaf Index	GLIavg	$\frac{(G-R)+(G-B)}{2*G+R+B}$	RGB	2.5
Second-Order texture (GLCM)	Contrast	glcmCONavg	Grayscale/Brightness RGB	Grayscale/RGB	Native
	Correlation	glcmCORavg	Grayscale/Brightness RGB	Grayscale/RGB	Native
	Variance	glcmVARavg	Grayscale/Brightness RGB	Grayscale/RGB	Native
	Inverse Different Moment	glcmIDMavg	Grayscale/Brightness RGB	Grayscale/RGB	Native
	Entropy	glcmENTavg	Grayscale/Brightness RGB	Grayscale/RGB	Native
Geometric	Area in hectares	Areaha	–	Segmented layer	–
Terrain	Slope	SLPavg	–	Digital Terrain Model	5
	Aspect	ASPavg	Reclassified in N, E, S, W, and flat	Digital Terrain Model	5
	Elevation	ELEavg	–	Digital Terrain Model	5
	Topographic Position Index	TPIavg	Weiss (2001)	Digital Terrain Model	5
	Minimum distance to sea	MDSavg	–	Distance to sea raster	5

Layers are the grayscale images of 1956 and 1989, the RGB image of 2021 and the LiDAR-based digital terrain model of 2019 at 5-m pixel resolution. R, red; G, green; B, blue. GSD: Ground sampling distance

Table 5 Summary of the training dataset per land class

		1956				1989				2021			
		Polygons		Area		Polygons		Area		Polygons		Area	
		#	%	ha	%	#	%	ha	%	#	%	ha	%
Land class	DFL	162	16.8	8231	39.4	564	38.8	6782	48.2	184	22.1	18,463	63.6
	SFL	88	9.1	249	1.2	409	28.1	2,027	14.4	242	29.1	8270	28.5
	TAL	296	30.5	206	1.0	66	4.5	130	0.9	84	10.1	221	0.8
	NTAL	222	22.9	12,056	57.7	312	21.4	4,902	34.8	108	13.0	393	1.4
	RGL	35	3.6	59	0.3	53	3.6	162	1.1	140	16.8	1577	5.4
	OTH	160	16.5	92	0.4	51	3.5	79	0.6	75	9.0	104	0.4
All classes		963	100	20,893	100	1455	100	14,082	100	838	833	100	29,029

'#' indicates the number of polygons in each class, while '%' represents the percentage that each class contributes to the total number of polygons

was used, downloadable in vectorial format from the IGN webpage https://centrodedescargas.cnig.es/CentroDescargas/catalogo.do?Serie=CAANE.

Random Forest polygon-based classification

Random Forest (RF) algorithms were used to classify LULC in the segmented polygons, which is a combination of classification and regression trees (CARTs) that work together to provide the expected value or class for target variable (Breiman et al. 2017). In remote sensing, this algorithm is widely used for image processing, both for pixel (e.g., Zhou et al. 2021; Langenkamp and Rienow 2023), or polygon (e.g., Dornik et al. 2018; Maxwell et al. 2019) classification. This machine learning algorithm follows a bootstrap strategy where a random subsample of the independent variables and another random subsample of the observations are used to build several CARTs, which then are averaged together to build the final RF model and is considered especially suitable for land classification tasks (Gómez et al. 2016). The final model is validated against the remaining observations, also known as an out-of-bag (OOB) validation. In our work, the RF model was built with the "ranger" R package (Wright and Ziegler 2017) and the model hyperparameters were fine-tuned with the "tuneRanger" R package (Probst et al. 2019). The model training process was repeated for each segmented orthophoto, resulting in an independent classification model for each (Table 6).

To deal with imbalanced classes in the training data (Table 5) a balanced random forest (BRF) algorithm was implemented, feeding the algorithm with the corresponding class weights (More and Rana 2017) in order to apply a stratified data bootstrap sampling method.

The predictive performance of the random forest models was assessed with the OOB prediction error and the confusion matrixes, from which the Kappa statistic (which rates the inter-rater reliability considering the possibility of the agreement occurring by chance) was obtained using the "epiR" R package (Stevenson et al. 2023). In order to estimate the stability of the model and flag potential overfitting problems, a fivefold cross-validation procedure was performed, reporting the test values and obtaining mean and standard deviation values for the overall accuracy and predictive power of the model. Variable importance calculations were implemented using the R package "iml" (Molnar et al. 2018) by comparing the classification error between the original and the shuffled models (i.e., trained model vs. model trained with random values assigned in the target variable to generate noise). Finally, we visually inspected the classified LULC layer and manually adjusted the most obviously misclassified segmented polygons after a random visual exploration across the study area, as it has been shown how thoughtful post-processing can substantially improve the final product (Reyes-Palomeque et al. 2021).

Table 6 Hyperparameters of each of the random forest models built per each photo

Year	Num. trees	Num. variables	Min. node size	Sample fraction	Replacement
1959	2000	5	5	0.8171333	False
1989	2000	5	5	0.7917714	FALSE
2021	2000	8	5	0.8151259	FALSe

Number of trees built in the forest, the number of variables with which each tree is built, and the minimum node size to split. No replacement was used

Assessing forest cover change over time

Once the LULC classifications were generated for each orthophoto (1956, 1989, and 2021), the LULC layer was reclassified into three categories, given that we wanted to specifically focus on the forest/agricultural covers evolution. To do so, the categories DFL and SFL were merged into forested land (FL), NTAL and TAL into agricultural land

(AL) and RGL and OTH into other (OTH). Forest age was estimated as a series of age classes based on the plausible range of dates for forest colonization given the timing of the orthophotographs, accounting for the most recent appearance of forest-classed pixels (Table 7). Finally, a pixel-wise map of forest age class as of 2021 based on the 2021 forest cover classification map was created.

To define these time intervals, two parameters were fixed: (1) the maximum forest age that can be assumed for naturally regenerated Aleppo pine forests in Ibiza, which was set at 120 years based on previous research (Del Río et al. 2008; Di Filippo et al. 2021) and our own data exploration; and (2) the minimum amount of time that a parcel of land needed to be effectively colonized by the forest to be photo interpreted as such, which was assumed to be 10 years based on visual exploration of the three orthophotos, expert criteria, and knowledge of the study region.

To compare the remotely sensed estimates of forest stand age to ground-based field data, a plot-based ground forest inventory dataset (N = 154, Fig. 2) was established between October 2021 and May 2024 in the area of interest. Plots were defined by a 10-m radius of a central point and all live trees with a diameter at breast height (DBH) equal or higher than 7.5 cm inside the plot were measured with a diameter

Table 7 Methodology to assign an age class to the forest age layer based on the pixel value of the 1956, 1989 and 2021 reclassified LULC layer

Orthophoto year/age classes	Forest LULC class			
1956	FL	non-FL	non-FL	FL
1989	FL	FL	non-FL	non-FL
2021	FL	FL	FL	FL
Minimum age (years)	75	42	10	10
Maximum age (years)	120	74	41	41
Average age (years)	97.5	58.0	25.5	25.5
Forest age class	A	B	C	C

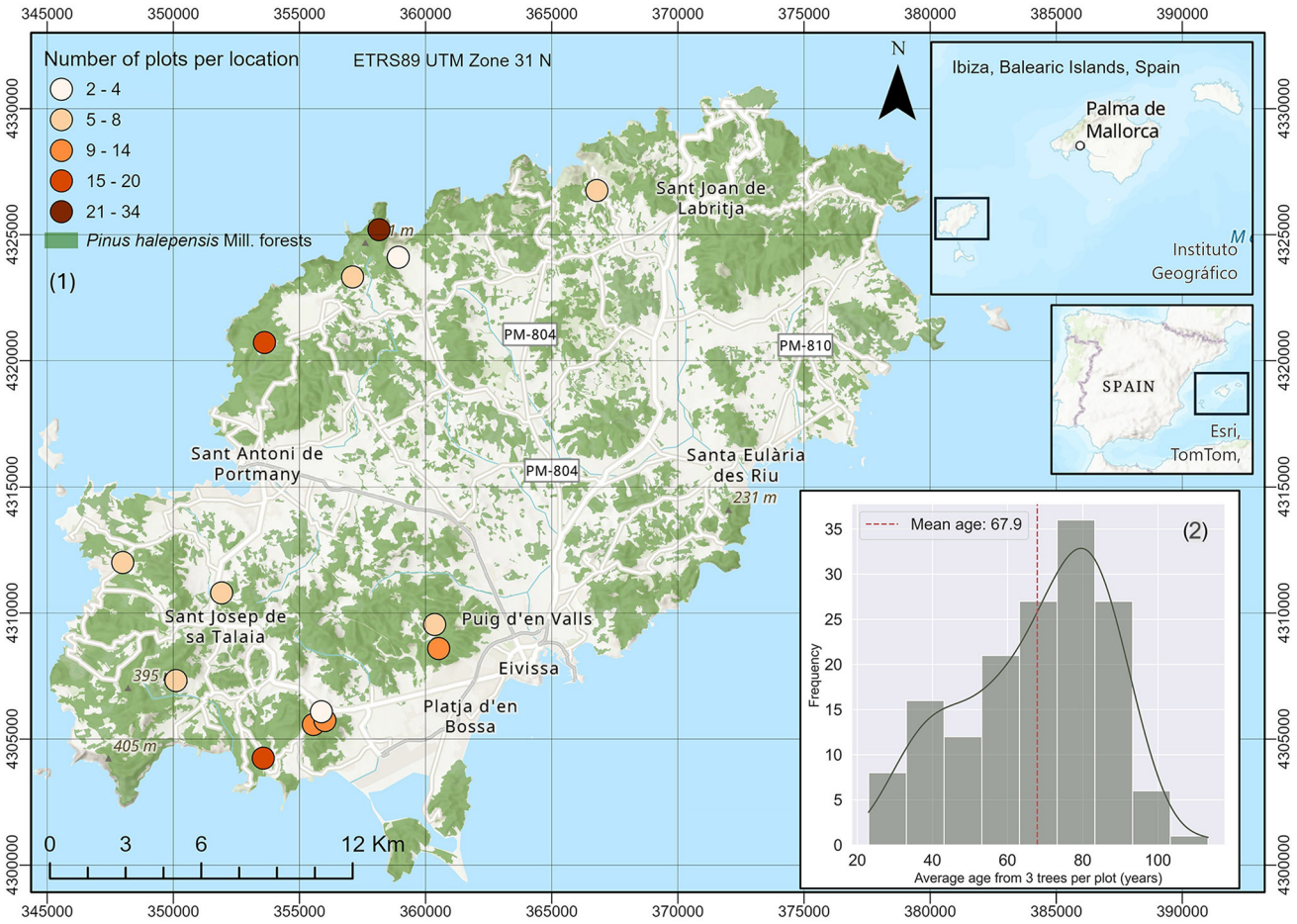


Fig. 2 Location of the forest inventory plots used as an internal validation of the remotely sensed method for forest age estimation (1). The inset represents the histogram of the average age using the three thickest trees per plot used in the study (2). The *P. halepensis* Mill. coverage has been extracted from the IV National Forest Inventory Map National Forest Map 1: 25,000 (2007–2017) (MAGRAMA 2012)

tape (Weiss, Germany). The three largest-DBH trees per plot were cored using a standard increment borer (Hagolf, Sweden) and stand age was approximated as the average tree age per plot (Fig. 2, inset 2). We retrieved the forest age class from the final raster layer obtaining the most common pixel value within each 10-m radius plot. Finally, Tukey's Honest Significant Difference (HSD) tests were employed (alpha = 0.05) to determine if there were discernible differences among ground-measured ages when categorized according to the age classifications obtained from our approach. The number of plots whose average age value accurately aligned to the forest age class interval was also assessed. Prior to this validation, the plot-level forest age averages were brought to 2021 from their original date of measurement.

The last step of the methodology consisted in the digitization of the largest wildfires since mid-twentieth century (the only areas where a precise forest age could be known, assuming a successful regeneration of the forest cover), and therefore reducing age uncertainty. We used the wildfire historic record (CMAT 2015), as well as a time series of HAPs and orthophotos ranging from 1956 and 2023. To more accurately identify unburnt areas within the most recent historical wildfire scars, low-density PNOA LiDAR data were used (either 2014 or 2019 flights) and applied a mask to the burn scar. The mask identified areas based on the above-ground height of the returns: pixels with return heights greater than 5 m indicated unburnt vegetation, while those with return heights below 5 m indicated areas where the fire had successfully consumed the trees, and therefore forest regeneration could be expected. The imagery was available on the Cartography and Geography Institute of Balearic Islands online visor (https://ideib.caib.es/visor/#) and the LiDAR data was downloaded from the Centro Nacional de Información Geográfica online servers, and processed locally following the same procedures as shown in Ribas-Costa et al. (2024) (https://centrodedescargas.cnig.es/CentroDescargas/index.jsp#). As an additional source of information, Landsat 1 and 2 satellite imagery available on Google Earth Engine was also used to manually identify the year in which the spectral scar of the wildfire appeared based on the true color reflectance across time. We ended up manually adding 40 major historic wildfires (areas ranged between 0.3 and 1,438 ha). Then, the location and timing of these identified wildfires was used to manually restrict forest age determination in the final map.

Results

Image segmentation accuracy assessment

The building of the training dataset showed that the segmentation was of high quality, as of the original training polygons less than half had to be manually modified due to under-segmentation. Under-segmented polygons always represented less than 5% of the total area of the training polygons for all images (Table 8).

Regarding the 1956 HAP-based orthophoto, due to its lower quality compared to the other two, the majority of the training polygon corrections performed were due to under-segmentation. In contrast, the 1989 and 2021 images were sharper and of higher quality, so the segmentation process was of higher detail and suffered less from under-segmentation.

Land cover and land use modeling

Random forest models performance

For the 1956 image, the average Kappa value obtained from the fivefold cross-validation procedure was 0.761, with an average accuracy of 81.3% (Table 9). In addition, the low variability across folds (Kappa standard deviation of 0.024 and accuracy standard deviation of 1.92%) showed high stability, denotating a low risk of overfitting. However, confusion between TAL and SFL, NTAL and DFL in flat areas or TAL and DFL in hillsides were the most common errors. After reclassifying the LULC classes into the simplified three-class scheme, the fivefold cross-validated Kappa was 0.791 with an accuracy of 87.5%. Regarding the 1989 image, the average Kappa value was 0.636, with an average accuracy of 74.0%. The variability across folds was higher compared to the previous 1956 image, with an average standard deviation of Kappa and accuracy of 0.045 and 3.46% respectively. Once we had reclassified cover into the three-class system of FL, AL or OTH LULC classes, the

Table 8 Quality reports of the segmentation procedure, performed to the training dataset systematically selected with the 1-km side grid. Number and representative area of polygons that had to be modified

Year	1956				1989				2021			
	Polygons		Area		Polygons		Area		Polygons		Area	
	#	%	ha	%	#	%	ha	%	#	%	ha	%
Accuracy	319	33.0	241.0	1.2	152	15.1	626.9	4.8	93	11.1	342.9	1.2

'#' indicates the number of polygons that had to be modified, while '%' represents the percentage that those polygons contributed to the total number of polygons interpreted

Table 9 Results of the fivefold cross-validation accuracy for the RF models for each photo before and after the LULC simplification

Year	6-class LULC statistics		3-class LULC statistics	
	Kappa	Overall accuracy (%)	Kappa	Overall accuracy (%)
1956	0.761 ± 0.024	81.3 ± 1.92	0.791 ± 0.012	88.9 ± 0.46
1989	0.636 ± 0.045	74.0 ± 3.46	0.776 ± 0.046	89.4 ± 2.25
2021	0.659 ± 0.032	72.6 ± 2.54	0.729 ± 0.039	82.4 ± 2.44

Numbers represent the mean value plus/minus one standard deviation. Uncertainty values obtained as one standard deviation of the results across the cross-validation folds

Kappa value rose to 0.776 and the accuracy to 89.4%. As before, some misclassification errors were present between TAL-FL and RGL-NTAL yet represented a low fraction of the total landscape. Finally, the 2021 image presented Kappa and accuracy values similar to the ones obtained in 1989: the average Kappa value prior to the LULC reclassification was 0.659, and the average accuracy was 72.6%. The standard deviation across folds was 0.032 for the Kappa estimate and 2.54% for the model accuracy. After reclassification to three classes, the reported values increased up to 0.729 and 80.7% for Kappa and overall accuracy, respectively. Although the previously stated misclassification errors were still present, a visual inspection of the predicted layers confirmed that the obtained performance was adequate to continue, and the final maps of LULC demonstrated to be highly representative of the landscape and its changes (Fig. 3).

Random forest model variable importance

The most important variable for the random forest model in the 1956 image was average slope, followed by mean distance to the sea (MDSavg) and GLCM average correlation (glcmCORavg) (Fig. 4). The mean gray value (GRAYavg) was the next variable in the ranking, followed by the mean topographic position index (TPIavg), and the area of each polygon (Areaha). Polygon aspect, as well as GLCM variance (glcmVARavg) and the standard deviation of the gray level (GRAYstd), had central positions in the ranking, whereas the rest of the GLCM metrics and elevation (ELEavg) were ranked as the least important features. Similarly, in the 1989 orthophoto average slope (SLPavg) and the mean gray value (GRAYavg) were ranked as the two most important features, yet their importance increased when compared to their importance in the 1956 orthoimage. As in the earlier image, mean distance to the sea (MDSavg) and the GLCM correlation metric (glcmCORavg) were the next most important variables. The rest of the DTM-based variables (ASPavg, TPIavg, and ELEavg) were ranked in the central positions, also similar to the 1956 image. However, both area (Areaha) and the standard deviation of the gray level (GRAYstd) were ranked in a lower position respect to the previous image. Finally, in the 2021 image, which included actual RBG spectral information, the NGRD Index (NGRDIavg) clearly outranked the other variables in importance, followed again by mean distance to sea (MDSavg) and slope (SLPavg). Unlike in previous images, in 2021 image the GLCM inverse different moment (glcmIDMavg) was ranked above other variables, although like the previous images GLCM average correlation (glcmCORavg) was also ranked as the next most important second-order texture analysis.

Forest change over time and forest age classification

There was a clear trend in forest cover increase since 1956 measured from the three-class LULC layers (Table 10, Fig. 5). In 1956, there were 21,165 ha of forest land (37.0% of the island area) and 36,059 ha of non-forest cover (63.0% of the island area). In 1989, the forest land had increased almost up to 27,099 ha, representing 46.8% of the total island. There was an additional forest cover increase between 1989 and 2021, in this case, over 3,000 ha. The mean annual increment was 139 ± 6 ha of forestland per year since 1956.

After combining the cover classes into FL/AL/OTH, and assessing forest age classes on the map, we observed that 17,379 ha of forest land corresponding to age class A (120–75 year), whereas only 6,120 ha and 6,680 ha corresponded to class B (74–42 years) and class C (41–10 years), respectively. When visually exploring the resulting layer, we confirmed that the methodology had sufficient resolution to capture fine-scale forest cover evolution successfully (Fig. 5). However, the land cover classification model could not effectively capture the effect of wildfires occurring between imagery acquisitions, which compelled the inclusion of the layer of historical wildfires as a final step. Finally, when comparing the means for the plot ages in forests marked Class A, Class B, and Class C, the Tukey's HSD test showed significant differences between all classes (p-value < 0.0001, Fig. 6). When looking at the actual means for each group (Table 10), Average age means for forest plots in each Class differed from the remotely sensed theoretical class central value by an average of 13 years. However, 63.0% of the ground plots exhibited an average measured age that accurately aligned with the forest age class identified through the remote sensing method (Table 11).

Closer examination of plots not aligned with their corresponding remotely sensed age class revealed that 22% of discrepancies stemmed from misclassifications within the LULC models in either 1956 or 1989. Additionally, 20% of age mismatches resulted from inadequate detail in orthophoto interpretation. For example, instances where the LULC model erroneously identified forest cover on scrubland or shadowed valley agricultural terraces were identified as forest cover in 1956, leading them to falsely register as higher age classes than actual. Another 13% of discrepancies occurred due to ground plot locations falling within transitional zones between forest and non-forest areas in either 1956 or 1989. Thus, despite accurate LULC model functioning in these cases, tree measurements were confined to a specific plot area, skewing results. Lastly, 44% of mismatches could be attributed to potential underestimation of age based on field data error, in which both the earlier and the latest tree rings in core samples can be more easily missed.

Discussion

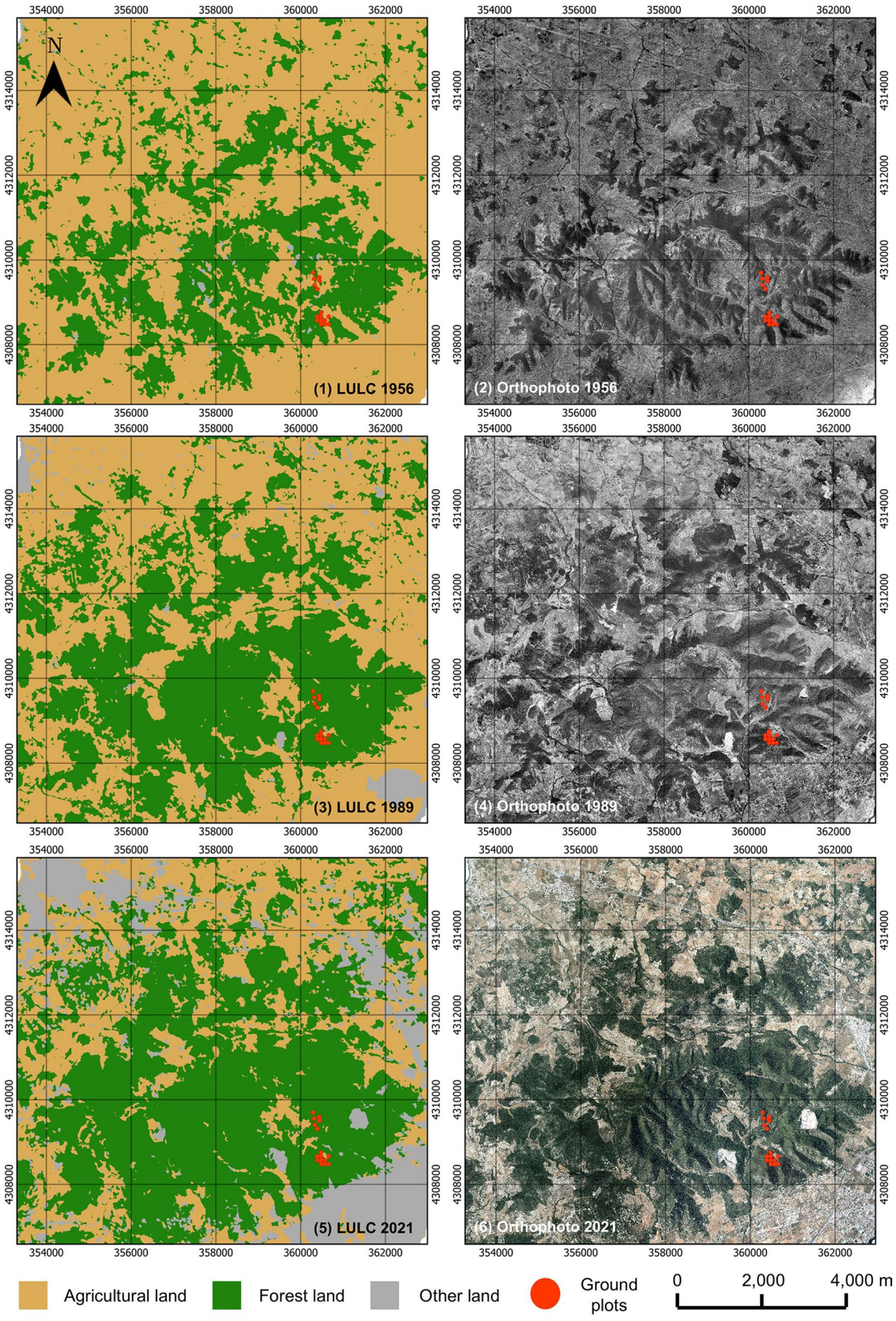
Random forest modeling for LULC

The performance of the models in this study was in line with other research: all our models reported an overall accuracy > 70% prior to LULC classes simplification and > 82% after applying the three-class LULC system. Other studies also following GEOBIA workflows have reported similar accuracies: Van der Broek et al. (2022) presented an overall accuracy of 69% when mapping 1981 land cover using HAP and a 14-level LULC map; Dornik et al. (2018) was able to distinguish 10 different soil types with terrain and multispectral satellite imagery with an accuracy of 54%; and Maxwell et al. (2019) mapped six current LULC classes using modern orthophotography and ancillary data, achieving an final accuracy of 98%. Nguyen et al. (2024) utilized a deep learning approach to map forest evolution in the Swiss Alps using a multi-temporal dataset of 13 orthophotos. They achieved F1 scores ranging from 0.8 to 0.9, which are in agreement with our results. Somewhat surprisingly, we achieved the highest accuracies with the older images, which can be attributed to more homogenous structure within land cover classes present in historical images. As the quality and resolution of the images increases with newer sensing technology (Maxwell et al. 2019) segmentation becomes more complex and must adapt to a more variant (and noisy) image landscape.

Regarding variable importance, rankings were substantially consistent across the different years. In the two HAP-based orthophotos, both gray level and slope were found to be among the most important features. This phenomenon was in agreement with our expectations, as forests, especially in the first half of the twentieth century were restricted to the soils less suitable for agriculture, i.e., mountain and remote areas (Rojas-Briales et al. 2018). This, as well as the fact that forests have a darker footprint than agriculture land, was successfully disentangled by the RF models in all cases and was consistent with Maxwell et al. (2019) findings. GLCM analysis also was substantially informative, as also suggested by other studies (Dornik et al. 2018; Maxwell et al. 2019; Langenkamp and Rienow 2023). When RGB image is available, it is clear that the vegetation indices that can be constructed with the visible bands aid substantially in object classification, in our case shifting the information retrieval mainly towards the NGRD Index. These results imply that a great deal of information useful for object segmentation and land cover classification is gained with the addition of multiple spectral bands compared to single-band panchromatic imagery, even with high spatial resolution. This was also observed in similar studies where additional spectral information increased the predictive performance of the model (Maxwell et al. 2019; Wang et al. 2019; Zhou et al. 2021; Atik and Ipbuker 2021; Nguyen et al. 2024). Finally, it is worth noting that land class Mean Distance to Sea had high importance rank because almost all OTH training polygons, representing either beaches or large urban areas, were located close to the sea.

Forest cover evolution and forest age class mapping

Several studies have used historical aerial or spaceborne imaging as a reliable source of information for historic, cultural, sociological, or urban studies (e.g., Pinto et al. 2019; Różycki et al. 2023; Pons and Rullán 2014b), to map land cover evolution driven by human (e.g., Nita et al. 2018) or natural processes (e.g., Van den Broeck et al. 2022; Knuth et al. 2023; Morford et al. 2024). Other studies have attempted to estimate and map forest age (Maltman et al. 2023), as it has been shown that knowledge of forest age is critical for understanding and managing forest ecosystems. However, current methodologies for forest age mapping are based on two major approaches: (1) a retrieval of a direct tree measurement (e.g., tree height) and the estimation of tree age based on inverted allometric equations (e.g., Véga and St-Onge 2009); or (2) the modeling of the forest age, either with structural parameters (e.g., Bey et al. 2016) or with its spectral properties (e.g., Reyes-Palomeque et al. 2021). However, as previously noted, these methodologies were restricted to the existing satellite imagery records. Fewer studies have used HAP as an additional source of information to identify tree cover expansion or reduction (e.g., Różycki et al. 2023; Morford et al. 2024) and we are aware of only one that uses more than two acquisitions (Nguyen et al. 2024). However, to our knowledge, no published work has yet advanced to the stage of translating and


N
(1) LULC 1956
(2) Orthophoto 1956
(3) LULC 1989
(4) Orthophoto 1989
(5) LULC 2021
(6) Orthophoto 2021
354000
356000
358000
360000
362000
4314000
4312000
4310000
4308000
Agricultural land
Forest land
Other land
Ground plots
0
2,000
4,000 m

◂**Fig. 3** Detail of the final LULC maps (left) and the original orthophoto (right) for a southeastern region of the Ibiza Island. Plots from the ground forest inventory in red, in this case corresponding to the ones closest to Puig d'en Valls and Eivissa in Fig. 2. Forest land class joins dense and sparse forest land covers; agricultural land class joins terraced and non-terraced agricultural land; and other land class englobes all the other land classes, namely: rocky grass lands, impervious surfaces, urban development, cliffs, beaches, etc.

validating orthophotography-based forest evolution into forest age classes, leaving this area largely unexplored.

In this work, we leverage the use of aerial photography series as a reliable source of information for forest age classification, by showing a substantial alignment between the remotely sensed forest age classes and the ground-measured age. Even though we could have attempted to obtain the Digital Surface Models (DSM) from the Structure from Motion (SfM) reconstruction of the original HAP photograms, we deemed that unnecessary as (1) the relation of forest height (both average height and its intrinsic variability) is weaker in Aleppo pine forests and across all ages, when compared to other forested lands, and (2) obtaining those raw photograms and their acquisition details (i.e., focal length, flight attitude, etc.) can sometimes be difficult (or impossible if those are lost). In this scenario, we believe that the presented methodology offers an alternative and functional way of using HAP-based orthoimages for land

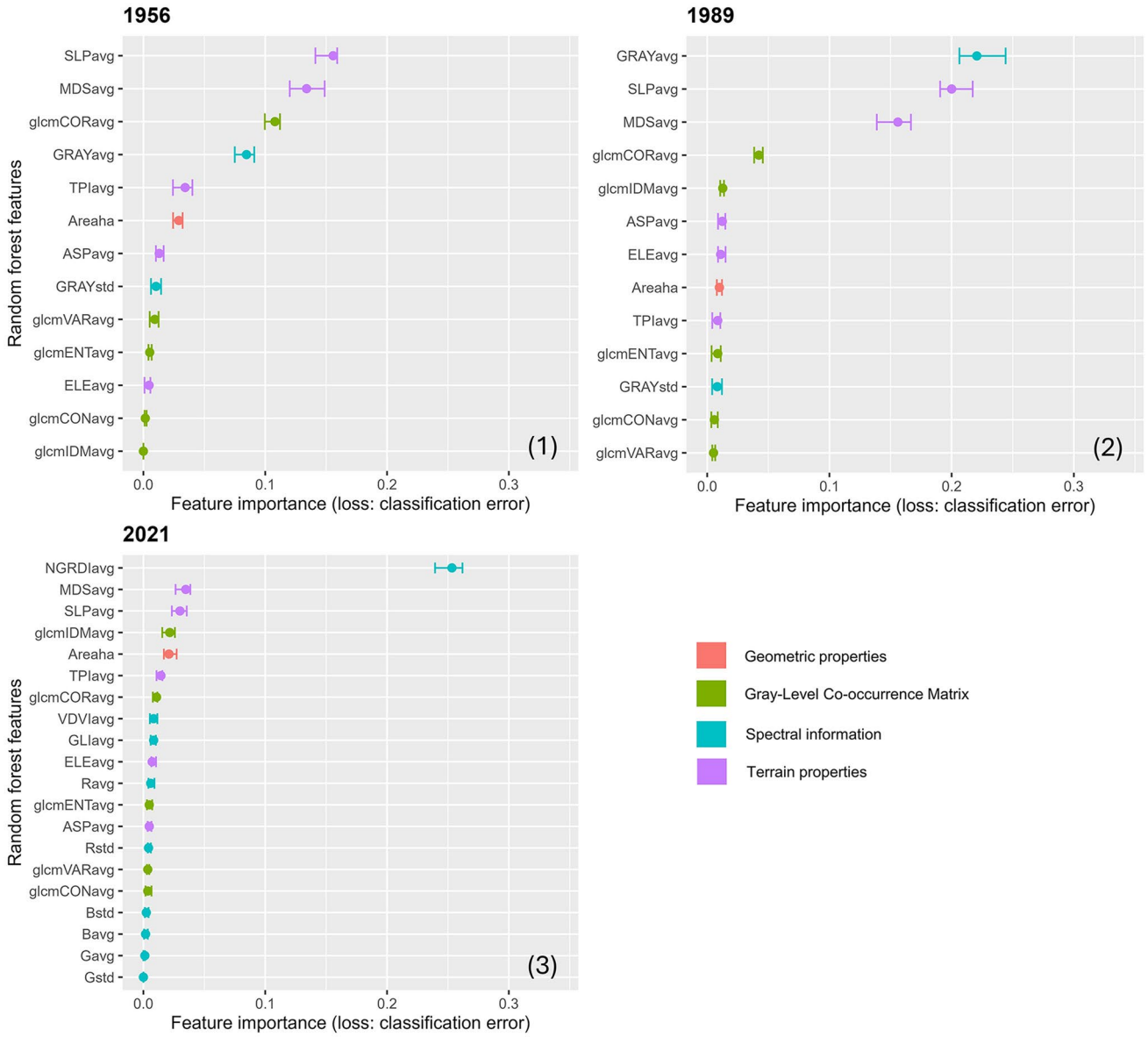


Fig. 4 Variable importance rankings for the 1956, 1989, and 2021 random forest models. Results represent the mean, 5th and 95 th quantiles of importance values from the repetitions. The classification loss is reported in absolute difference between the original model and the model with the shuffled variable

cover evolution, and specifically, discrete forest age mapping. Despite the fact that the methodology is restricted to a discrete classification of forest age classes, we show how the theoretical age classes generated with the series of orthophotos align well with the ground measurements. The mean deviation from the remotely sensed forest age mean value and the ground-measured forest age is 13 years. This error cannot be directly compared to other continuous-scale methodologies, as it assumes that all stands within an age class are exactly at the midpoint of that age range (which ground forest inventory shows is not accurate). However, despite this limitation, the results are still consistent with those from other studies, which can range from 5 to 50 years (Kayitakire et al. 2006; Véga and St-Onge 2009; Frate et al. 2016; Bey et al. 2016; Maltamo et al. 2020; Schumacher et al. 2020; Reyes-Palomeque et al. 2021). Forest stand age studies like these are normally based on the strong relationship between stand age and forest height (Véga and St-Onge 2009; Vastaranta et al. 2016; Maltman et al. 2023). However, for mature Mediterranean Aleppo pine forests this relation can be weaker, especially if the uneven-aged distribution of the canopy is reached once the trees lose apical dominance (Alberdi et al. 2013; Bey et al. 2016). It is also important to acknowledge that while tree cores are commonly regarded as the most precise method for determining tree age, even this approach is subject to a margin of error typically ranging from 10 to 20 years (Koch et al. 2008; Fraver et al. 2011; Metsaranta 2020). In this work, no laboratory-based dendrochronological analysis was performed, yet this analysis has been shown to improve tree-ring estimates, especially when missing rings are present (Bachtobji et al. 2017; Di Filippo et al. 2021). Missing ring artifacts could help explain the percentage of plots identified to be in the oldest forest age class but estimated to be younger. Accordingly, although improving the accuracy of the validation data would improve the uncertainty estimates, we do not consider this to be a limitation of the methodology, particularly considering the wide time intervals of 33 years between orthophotos and our forest age estimation accuracy.

Table 10 Evolution of the forest and other land covers from 1956 to 2021 based on our results

Year	Forested land cover classes		Rest of land cover classes	
	ha	%	ha	%
1956	21,165 ± 252	37.0 ± 0.4	36,059 ± 252	63.0 ± 0.4
1989	27,099 ± 472	46.8 ± 0.8	30,784 ± 472	53.2 ± 0.8
2021	30,195 ± 302	52.8 ± 0.5	27,049 ± 302	47.3 ± 0.5

Uncertainty values obtained as one standard deviation of the predicted forest cover across the cross-validation folds

'%' represents the percentage that each land class contributes to the total area of the island in each year

Regarding the forest cover estimates, our results are in line with those already published. In 1956, we estimated that 37% of the island of Ibiza was covered by forests, and other studies suggest that it was even lower at 20% during the first half of the twentieth century (Roig-Coll and Kechagia 2022). Currently, we estimated a forested cover of 30,195 ha in 2021, whereas the IV Spanish National Forest Inventory estimated 29,914 ha in 2012 (MAGRAMA 2012), and the EU observatory on deforestation and forest degradation estimated 27,576 ha in 2020 (Joint Research Centre 2020). This LULCC and the previous forest age distribution reflects the trends already observed in other mediterranean environments in the past century: the transition to a more homogeneous landscape based on the abandonment of agriculture and other livestock areas (Camarero-Rioja 1991; Lasanta-Martínez et al. 2005; González-Ávila et al. 2020; Amezteguí et al. 2021; Delgado-Artés et al. 2022). Though we did not perform a full analysis of the socioeconomic and demographic factors that derived in these LULCCs, there are major aspects to consider in order to better understand the forest expansion. When narrowing the scope to Ibiza in the twentieth century, the local agricultural economy depended largely upon the exports of salt, almonds, eggs, and lumber (Cirer-Costa 2023) combined with very intensive production of other agricultural or forest products for local self-consumption. Accordingly, the structure of the landscape was the result of a very intensive land use, which pushed the forestland towards the most topographically complex terrain unsuitable for agriculture (Fox et al. 2012; Rojas-Briales et al. 2018). Despite the fact that the first agricultural abandonment happened in late 19 th to early twentieth century, when emigration levels raised as a result of the harsh conditions found on the island (Cirer-Costa 2023), major land abandonment accelerated in the mid-twentieth century as a result of the arrival of tourism (Pons and Rullan 2014b). Irrespective of the moment of the abandonment, these patterns of change acted within Ibiza's forests alleviating the pressure that had constrained them to the higher elevations of the mountains for decades, facilitating a "radial" expansion of forested areas. An illustration of this phenomenon is evident when examining Fig. 5.

Consequently, and over the past 50 years, the island's economy has shifted from agriculture to being primarily tourism-based, adding complexity to socio-economic and natural dynamics. Both the growth rate and the overall increase in forest cover has far-reaching impacts in today's context. On the one hand, it has led to a decline in agricultural production due to farmland abandonment and the consequent conversion of fertile land to forest or developed (urban) land. On the other hand, however, this newly grown forest has tremendous productivity potential as it grows on

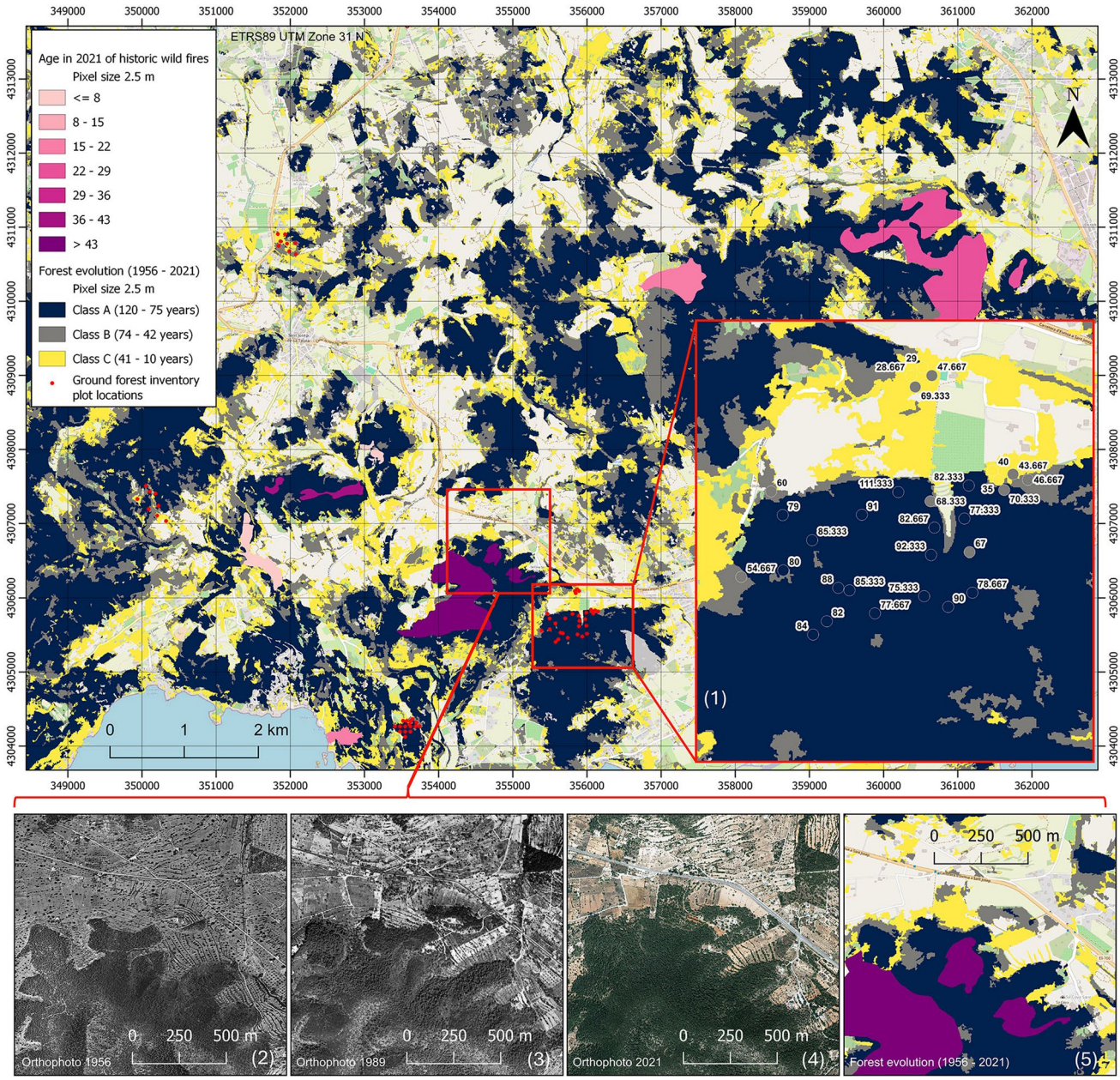


Fig. 5 Forest evolution (yellow, gray, and blue) based on the methodology presented, after including the historic wildfires layer (in pink-purple color scale). Inset (1) shows the plot-level forest inventory average age for one of the forest inventory data locations, and insets (2–5) show a zoom in for all years at an example location

high quality soils (Ribas-Costa et al. 2024), which affects carbon sequestration and timber potential. This shift has also caused habitat loss for species like the red-legged partridge (*Alectoris rufa* L.) (e.g., Delibes-Mateos et al. 2012), increased wildfire risks due to continuous forest expansion (e.g., Castellnou et al. 2007), and intensified water uptake contributing to reducing forest's resistance to drought conditions (e.g., Sohn et al. 2016). Alternatively, the increase in forest cover in a catchment area has proven beneficial to reduce the hydrological discharge, flood generation, and sediment transport (García-Ruiz et al. 2008; Martínez-Fernández et al. 2017).

Limitations and further directions

In terms of forest age mapping, our study's main limitation is that we present a discrete scale of forest age rather than a continuous map for this parameter. This study used three images (1956, 1989, and 2021), giving us a 33-year interval among acquisitions and limiting the number of discrete

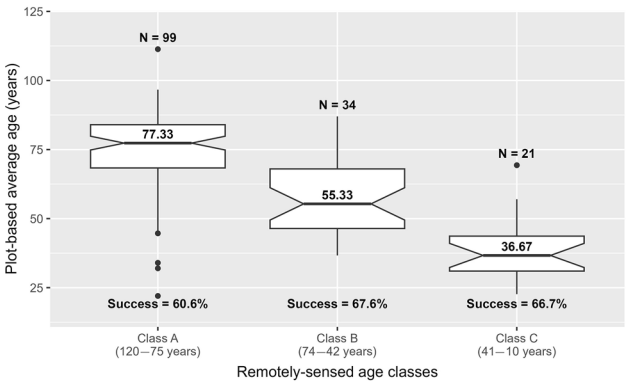


Fig. 6 Boxplots to represent the differences between the different remotely sensed age classes and the ground-based forest inventory age data. The dark line represents the median value, the notch are the confidence intervals, and the whiskers represent ± 1.5 the interquartile range. The success value is the percentage of plots whose average age fell within the age range of each remotely sensed age class

Table 11 Validation results of the comparison between the remote sensing -based methodology to obtain forest age and the ground forest inventory data

Forest age Class	Theoretical mean (years)	Ground average age (years)	Difference (years)
Class A: 120–75 years	97.5	74.5 A	23.0
Class B: 74–42 years	58.0	57.0 B	1.0
Class C: 41–10 years	25.5	40.5 C	15.0

Different letters indicate significant differences among groups

age classes we could discern. We discarded the use of more images taken in between because more HAP-based imagery was not fully available between 1956 and 1989, and those that did exist needed to be orthorectified and were either of lower quality or had incomplete coverage. Furthermore, in this study we were attempting to capture forest cover re-colonization, which is a relatively slow process, and accordingly having more intermediate image would potentially add noise to the forest cover estimates (Nguyen et al. 2024). However, this translates into the method relying on the assumption that forest age progresses linearly, which may not be the case in forests that are actively managed. Having only three periods implied that if a harvest occurred just after the first period, the second image would still be identified as forest cover, but the age would be overpredicted by the model. While this tendency may limit the applicability of the method elsewhere, we are confident that this risk was minimal in the area of interest, as there is little forest management. On the other hand, the limiting factor of having only three images to work with implied that we were much more reliant on the accuracy of each LULC model. In our case, the 1989 orthophoto was found to be irregularly overexposed/underexposed across the study area which affected the models and implied that a greater degree of manual post-processing had to be done to overcome misclassification errors. Despite these efforts, several misclassification errors were still found, which affected the final estimates of different land covers in each image. Nguyen et al. (2024) reported similar limitations even with their deep learning approach. However, in that case with the use of higher temporal resolution and the addition of multi-temporal information to the model, together with the implementation of a function to mimic the knowledge-based forest dynamics, helped with the automatic detection and correction of the errors.

Harmonizing different data sources (i.e., panchromatic and RGB imagery) was also a challenge. Manual adjustments on the pre-processing steps and segmentation hyperparameter fine-tuning had to be done in order to adapt the segmentation algorithm to work similarly in all three orthomosaics. However, the fact that lower accuracy was found in more modern imagery highlights a need for further improvement. After segmentation, the training dataset required manual photo interpretation, which presented several challenges. Among these, we highlight the difficulty of classifying abandoned agricultural fields as either forested or non-forested areas. Once agricultural activity ceases, the re-colonization of tree cover can happen at different rates and following different patterns (Ameztegui et al. 2021; Delgado-Artés et al. 2022), and this classification can be complex, both for humans and machine learning algorithms (Nguyen et al. 2024). In this study, we assigned segments as forested land if more trees than usual were found in it, making edge cases in some instances difficult to determine. Finally, we would like to note that despite the work performed to identify the bun scars only the outer contour of most of the wildfires was polygonised, but no manual photo interpretation of un-burnt patches inside the boundaries was performed. Therefore, not all the area within the wildfire perimeter might have the same age (especially in old large fires that burned irregularly). For new to-come wildfires, this source of error could be overcome by automatic satellite-based identification or new national LiDAR acquisitions; however, the majority of the wildfires mapped in this work happened prior to the advent of high-resolution multi-spectral satellite imagery or LiDAR.

This work aimed to develop and test a methodology to provide first-order estimates of the different age classes, and to test it in Ibiza's naturally regenerated pine forests. We found that the island has gained in average 139 ± 6 ha per year since 1956. These findings now open the door for a better understanding of the land cover change processes involved and provide evidence that high-resolution aerial imagery time series is an outstanding source of information to map forest evolution and understand its spatiotemporal patterns. Multiple lines of research arise

from this work at this point: on the one hand, this methodology could be extended to the neighboring Balearic Islands and study if the forest evolution patterns followed the same trends shown here. On the other hand, this forest age layer could be combined with biomass/volume or dominant height continuous layers to obtain forest productivity, either in terms of mean annual increment or site index. And finally, this study could be extended into the past by including historical references to forest cover in Ibiza, as shown in Kaim et al. (2016).

Conclusion

In this study, three orthophotos covering a time span of 66 years have been utilized to study the changes in land cover and land uses within that period. The potential of HAP and modern RGB aerial imaging as a reliable and valuable source of information to generate continuous maps of LULC for each of the three selected periods has been studied. We explored how both data types could be combined in order to explore and map forest evolution and assign forest age classes, providing an alternative way to achieve so without relying on SfM-based canopy height models. We found an annual gain of 139 ± 6 ha of forest cover since 1956, in line with other studies in the Mediterranean. This research not only enriches our comprehension of *P. halepensis* Mill. forest dynamics and land use/land cover evolution, but also highlights the capacity of high-resolution aerial imagery time series in delineating forest changes and clarifying spatiotemporal patterns. Accordingly, an accurate map delineating forest age categories has been produced, which will be accessible to stakeholders for enhancing forest management practices and informing regional landscape planning initiatives.

Acknowledgements We would like to thank the company Terrapi World Ltd. plus the landowners who shared the inventory data.

Author contributions Vicent A. Ribas Costa: Conceptualization, methodology, software, validation, formal analysis, data curation, investigation, writing—original draft, writing—review and editing, funding acquisition, visualization. Andrew Trlica: Methodology, writing—review and editing. Aitor Gastón: Methodology, validation, formal analysis, supervision, writing—review and editing.

Funding Open Access funding provided thanks to the CRUE-CSIC agreement with Springer Nature.

Data availability The PNOA LiDAR and 1956 and 2021 orthophotos are openly available at the Centro de Descargas of the Instituto Geográfico Nacional (https://centrodedescargas.cnig.es/CentroDescargas/index.jsp). The 1989 orthophoto is available under request at the Institut Cartogràfic i Geogràfic de les Illes Balears (https://www.caib.es/webgoib/institut-cartografic-i-geografic-de-les-illes-balears-icgib-). Forest inventory data is property of the landowners and managed by Terrapi World Ltd. Sharable data and scripts were deposited on Zenodo under.

Open Access This article is licensed under a Creative Commons Attribution 4.0 International License, which permits use, sharing, adaptation, distribution and reproduction in any medium or format, as long as you give appropriate credit to the original author(s) and the source, provide a link to the Creative Commons licence, and indicate if changes were made. The images or other third party material in this article are included in the article's Creative Commons licence, unless indicated otherwise in a credit line to the material. If material is not included in the article's Creative Commons licence and your intended use is not permitted by statutory regulation or exceeds the permitted use, you will need to obtain permission directly from the copyright holder. To view a copy of this licence, visit http://creativecommons.org/licenses/by/4.0/.

References

Alberdi I, Cañellas I, Hernández L, Condés S (2013) A new method for the identification of old-growth trees in National Forest Inventories: application to *Pinus halepensis* Mill. stands in Spain. Ann for Sci 70(3):277–285. https://doi.org/10.1007/s13595-012-0261-9

Almonacid-Caballer J, Pardo-Pascual JE, Ruiz LA (2017) Evaluating Fourier cross-correlation sub-pixel registration in landsat images. Remote Sens 9(10):1051. https://doi.org/10.3390/rs9101051

Ambrosio L, Alonso R (1993) Estimación de superficies cultivadas por muestreo de áreas y teledetección. Precisión Relativa Estadística Española 35(132):91–103 (**(in Spanish)**)

Ameztegui A, Morán-Ordóñez A, Márquez A, Blázquez-Casado Á, Pla M, Villero D, García MB, Errea MP, Coll L (2021) Forest expansion in mountain protected areas: trends and consequences for the landscape. Landsc Urban Plan 216:104240. https://doi.org/10.1016/j.landurbplan.2021.104240

Atik SO, Ipbuker C (2021) Integrating convolutional neural network and multiresolution segmentation for land cover and land use mapping using satellite imagery. Appl Sci 11(12):5551. https://doi.org/10.3390/app11125551

Bachtobji Bouachir B, Khorchani A, Guibal F, El Aouni MH, Khaldi A (2017) Dendroecological study of *Pinus halepensis* and *Pinus pinea* in northeast coastal dunes in Tunisia according to distance from the shoreline and dieback intensity. Dendrochronologia 45:62–72. https://doi.org/10.1016/j.dendro.2017.06.008

Bajocco S, De Angelis A, Perini L, Ferrara A, Salvati L (2012) The impact of land use/land cover changes on land degradation dynamics: a Mediterranean case study. Environ Manage 49(5):980–989. https://doi.org/10.1007/s00267-012-9831-8

Bakker MM, Veldkamp A (2008) Modelling land change: the issue of use and cover in wide-scale applications. J Land Use Sci 3(4):203–213. https://doi.org/10.1080/17474230802465181

Belward AS, Skøien JO (2015) Who launched what, when and why; trends in global land-cover observation capacity from civilian earth observation satellites. ISPRS J Photogramm Remote Sens 103:115–128. https://doi.org/10.1016/j.isprsjprs.2014.03.009

Bey A, Sánchez-Paus Díaz A, Maniatis D, Marchi G, Mollicone D, Ricci S, Bastin JF, Moore R, Federici S, Rezende M, Patriarca C, Turia R, Gamoga G, Abe H, Kaidong E, Miceli G (2016) Collect earth: land use and land cover assessment through augmented visual interpretation. Remote Sens 8(10):807. https://doi.org/10.3390/rs8100807

Blaschke T (2010) Object based image analysis for remote sensing. ISPRS J Photogramm Remote Sens 65(1):2–16. https://doi.org/10.1016/j.isprsjprs.2009.06.004

Bossard M, Feranec J, Otahel J (2000) CORINE land cover technical guide: addendum 2000. European Environment Agency, Copenhagen

Breiman L, Friedman JH, Olshen RA, Stone CJ (2017) Classification and regression trees. Apple Academic Press, Cambridge

Buddenbaum H, Schlerf M, Hill J (2005) Classification of coniferous tree species and age classes using hyperspectral data and geostatistical methods. Int J Remote Sens 26(24):5453–5465. https://doi.org/10.1080/01431160500285076

Büttner G, Feranec J, Jaffrain G, Mari L, Maucha G, Soukup T (2004) The CORINE land cover 2000 project. EARSeL eProceedings 3:331–346

Camarero-Rioja LA (1991) Tendencias recientes y evolución de la población rural en España. Política y Sociedad 8:13–24

Castellnou M, Nebot E, Miralles M (2007) El papel del fuego en la gestión del paisaje. In: 4th International Wildland Fire Conference. Sevilla, pp. 13–17. **(in Spanish)**

Castilla G, Hay GJ (2008) Image-objects and geographic objects. In: Blaschke T, Lang S, Hay GJ (eds) Object-Based Image Analysis. Springer, Heidelberg, pp 91–110

Chen G, Thill JC, Anantsuksomsri S, Tontisirin N, Tao R (2018) Stand age estimation of rubber (*Hevea brasiliensis*) plantations using an integrated pixel- and object-based tree growth model and annual Landsat time series. ISPRS J Photogramm Remote Sens 144:94–104. https://doi.org/10.1016/j.isprsjprs.2018.07.003

Chmielewski S, Bochniak A, Natapov A, Wężyk P (2020) Introducing *GEOBIA* to landscape imageability assessment: a multi-temporal case study of the nature reserve "Kózki." Poland Remote Sens 12(17):2792. https://doi.org/10.3390/rs12172792

Cirer-Costa JC (2023) Ibiza and the introduction of capitalism in the Mediterranean: from agrarian self-consumption to full market dependence, 1857–1935. Historia Agraria 89: 159–191. https://doi.org/10.26882/histagrar.089e03c

CMAT (2015) Conselleria d'Agricultura, Medi Ambient i Territori. IV Pla General de Defensa Contra Incendis Forestals de les Illes Balears. Govern de les Illes Balears, Tecnosylva SL.

Collantes F (2007) La desagrarización de la sociedad rural española, 1950–1991. Historia Agraria – SEHA 42: 251–276.

Costa H, Foody GM, Boyd DS (2018) Supervised methods of image segmentation accuracy assessment in land cover mapping. Remote Sens Environ 205:338–351. https://doi.org/10.1016/j.rse.2017.11.024

Das P, Pandey V (2019) Use of logistic regression in land-cover classification with moderate-resolution multispectral data. J Indian Soc Remote Sens 47(8):1443–1454. https://doi.org/10.1007/s12524-019-00986-8

Delgado-Artés R, Garófano-Gómez V, Oliver-Villanueva JV, Rojas-Briales E (2022) Land use/cover change analysis in the Mediterranean region: a regional case study of forest evolution in Castelló (Spain) over 50 years. Land Use Policy 114:105967. https://doi.org/10.1016/j.landusepol.2021.105967

Delibes-Mateos M, Farfán MÁ, Olivero J, Vargas JM (2012) Impact of land-use changes on red-legged partridge conservation in the Iberian Peninsula. Envir Conserv 39(4):337–346. https://doi.org/10.1017/s0376892912000100

Di Filippo A, Baliva M, Brunetti M, Di Fiore L (2021) Long-term tree-ring response to drought and frost in two *Pinus halepensis* populations growing under contrasting environmental conditions in peninsular Italy. Forests 12(3):305. https://doi.org/10.3390/f12030305

Dornik A, Drăguţ L, Urdea P (2018) Classification of soil types using geographic object-based image analysis and random forests. Pedosphere 28(6):913–925. https://doi.org/10.1016/S1002-0160(17)60377-1

Ez-zahouani B, Teodoro A, El Kharki O, Liu JH, Kotaridis I, Yuan XH, Ma L (2023) Remote sensing imagery segmentation in object-based analysis: a review of methods, optimization, and quality evaluation over the past 20 years. Remote Sens Appl Soc Environ 32:101031. https://doi.org/10.1016/j.rsase.2023.101031

Di Fazio S, Modica G, Zoccali P (2011) Evolution trends of land use/land cover in a mediterranean forest landscape in Italy. In: Murgante B, Gervasi O, Iglesias A, Taniar D, Apduhan BO (Eds.) Comp. Sci. Applic. - ICCSA 2011. ICCSA 2011. Lecture Notes in Computer Science 6782. Springer, Berlin, Heidelberg. https://doi.org/10.1007/978-3-642-21928-3_20

Fernández García F (2015) Fotografía aérea histórica e historia de la fotografía aérea en España. Ería 98(98):217–240

Fox DM, Witz E, Blanc V, Soulié C, Penalver-Navarro M, Dervieux A (2012) A case study of land cover change (1950–2003) and runoff in a Mediterranean catchment. Appl Geogr 32(2):810–821. https://doi.org/10.1016/j.apgeog.2011.07.007

Frate L, Carranza ML, Garfì V, Febbraro MD, Tonti D, Marchetti M, Ottaviano M, Santopuoli G, Chirici G (2016) Spatially explicit estimation of forest age by integrating remotely sensed data and inverse yield modeling techniques. Iforest 9(1):63–71. https://doi.org/10.3832/ifor1529-008

Fraver S, Bradford JB, Palik BJ (2011) Improving tree age estimates derived from increment cores: a case study of red pine. For Sci 57(2):164–170. https://doi.org/10.1093/forestscience/57.2.164

Fu Z, Li DJ, Hararuk O, Schwalm C, Luo YQ, Yan LM, Niu SL (2017) Recovery time and state change of terrestrial carbon cycle after disturbance. Environ Res Lett 12(10):104004. https://doi.org/10.1088/1748-9326/aa8a5c

García-Ruiz JM, Regüés D, Alvera B, Lana-Renault N, Serrano-Muela P, Nadal-Romero E, Navas A, Latron J, Martí-Bono C, Arnáez J (2008) Flood generation and sediment transport in experimental catchments affected by land use changes in the central Pyrenees. J Hydrol 356(1–2):245–260. https://doi.org/10.1016/j.jhydrol.2008.04.013

Gómez C, White JC, Wulder MA (2016) Optical remotely sensed time series data for land cover classification: a review. ISPRS J Photogramm Remote Sens 116:55–72. https://doi.org/10.1016/j.isprsjprs.2016.03.008

González-Ávila S, López-Leiva C, Bunce RGH, Elena-Rosselló R (2020) Changes and drivers in Spanish landscapes at the rural-urban interface between 1956 and 2018. Sci Total Environ 714:136858. https://doi.org/10.1016/j.scitotenv.2020.136858

González-Avila S, Elena-Rosselló R (2009) SISPARES: cartografía nacional del patrón y cambio de los paisajes rurales españoles. Cuadernos de la Sociedad Española de Ciencias Forestales 29: 15–21. https://doi.org/10.31167/csef.v0i29.9812

Gromada K (2022) Unsupervised SAR imagery feature learning with Median filter-based loss value. Sensors 22(17):6519. https://doi.org/10.3390/s22176519

Grottoli E, Biausque M, Rogers D, Jackson DWT, Cooper JAG (2021) Structure-from-motion-derived digital surface models from historical aerial photographs: a new 3D application for coastal dune monitoring. Remote Sens 13(1):95. https://doi.org/10.3390/rs13010095

Guzha AC, Rufino MC, Okoth S, Jacobs S, Nóbrega RLB (2018) Impacts of land use and land cover change on surface runoff, discharge and low flows: evidence from East Africa. J Hydrol Reg Stud 15:49–67. https://doi.org/10.1016/j.ejrh.2017.11.005

Heisig H, Simmen JL (2021) Re-engineering the past: countrywide geo-referencing of archival aerial imagery. PFG 89(6):487–503. https://doi.org/10.1007/s41064-021-00162-z

Joint Research Centre (2020) Global map of forest cover for year 2020. EU observatory on deforestation and forest degradation. European Commission.

Kaim D, Kozak J, Kolecka N, Ziółkowska E, Ostafin K, Ostapowicz K, Gimmi U, Munteanu C, Radeloff VC (2016) Broad scale forest cover reconstruction from historical topographic maps. Appl Geogr 67:39–48. https://doi.org/10.1016/j.apgeog.2015.12.003

Kayitakire F, Hamel C, Defourny P (2006) Retrieving forest structure variables based on image texture analysis and IKONOS-2 imagery. Remote Sens Environ 102(3–4):390–401. https://doi.org/10.1016/j.rse.2006.02.022

Kennedy RE, Yang ZQ, Cohen WB (2010) Detecting trends in forest disturbance and recovery using yearly Landsat time series: 1 LandTrendr—Temporal segmentation algorithms. Remote Sens Environ 114(12):2897–2910. https://doi.org/10.1016/j.rse.2010.07.008

Knuth F, Shean D, Bhushan S, Schwat E, Alexandrov O, McNeil C, Dehecq A, Florentine C, O'Neel S (2023) Historical structure from motion (HSfM): automated processing of historical aerial photographs for long-term topographic change analysis. Remote Sens Environ 285:113379. https://doi.org/10.1016/j.rse.2022.113379

Koch AJ, Driscoll DA, Kirkpatrick JB (2008) Estimating the accuracy of tree ageing methods in mature *Eucalyptus obliqua* forest. Tasmania Aust for 71(2):147–159. https://doi.org/10.1080/00049158.2008.10676281

Kwon SK, Jung HS, Baek WK, Kim D (2017) Classification of forest vertical structure in south Korea from aerial orthophoto and lidar data using an artificial neural network. Appl Sci 7(10):1046. https://doi.org/10.3390/app7101046

Langenkamp JP, Rienow A (2023) Exploring the use of orthophotos in google earth engine for very high-resolution mapping of impervious surfaces: a data fusion approach in Wuppertal. Germany Remote Sens 15(7):1818. https://doi.org/10.3390/rs15071818

Lasanta-Martínez T, Vicente-Serrano SM, Cuadrat-Prats JM (2005) Mountain Mediterranean landscape evolution caused by the abandonment of traditional primary activities: a study of the Spanish Central Pyrenees. Appl Geogr 25(1):47–65. https://doi.org/10.1016/j.apgeog.2004.11.001

Liu DS, Xia F (2010) Assessing object-based classification: advantages and limitations. Remote Sens Lett 1(4):187–194. https://doi.org/10.1080/01431161003743173

Liu XP, He JL, Yao Y, Zhang JB, Liang HL, Wang H, Hong Y (2017) Classifying urban land use by integrating remote sensing and social media data. Int J Geogr Inf Sci 31(8):1675–1696. https://doi.org/10.1080/13658816.2017.1324976

Liu K, Shen X, Cao L, Wang GB, Cao FL (2018) Estimating forest structural attributes using UAV-LiDAR data in *Ginkgo* plantations. ISPRS J Photogramm Remote Sens 146:465–482. https://doi.org/10.1016/j.isprsjprs.2018.11.001

Lu H, Liu C, Li NW, Fu X, Li LG (2021) Optimal segmentation scale selection and evaluation of cultivated land objects based on high-resolution remote sensing images with spectral and texture features. Environ Sci Pollut Res Int 28(21):27067–27083. https://doi.org/10.1007/s11356-021-12552-2

MAGRAMA (2012) Ministerio de Agricultura, Alimentación y Medio Ambiente. 4th Spanish national forest inventory. Dirección General de Desarrollo Rural y Política Forestal, Área de Inventario y Estadísticas Forestales.

Maltamo M, Kinnunen H, Kangas A, Korhonen L (2020) Predicting stand age in managed forests using National Forest Inventory field data and airborne laser scanning. For Ecosyst 7:44. https://doi.org/10.1186/s40663-020-00254-z

Maltman JC, Hermosilla T, Wulder MA, Coops NC, White JC (2023) Estimating and mapping forest age across Canada's forested ecosystems. Remote Sens Environ 290:113529. https://doi.org/10.1016/j.rse.2023.113529

Martínez-Fernández V, del Tánago MG, Maroto J, de Jalón DG (2017) Fluvial corridor changes over time in regulated and non-regulated rivers (upper esla river, NW Spain). River Res Appl 33(2):214–223. https://doi.org/10.1002/rra.3032

Maxwell AE, Strager MP, Warner TA, Ramezan CA, Morgan AN, Pauley CE (2019) Large-area, high spatial resolution land cover mapping using random forests, *GEOBIA*, and NAIP orthophotography: findings and recommendations. Remote Sens 11(12):1409. https://doi.org/10.3390/rs11121409

Metsaranta JM (2020) Dendrochronological procedures improve the precision and accuracy of tree and stand age estimates in the Western Canadian boreal forest. For Ecol Manag 457:117657. https://doi.org/10.1016/j.foreco.2019.117657

Molnar C, Bischl B, Casalicchio G (2018) *iml*: An R package for interpretable machine learning. J Open Source Soft 3(26):786

More AS, Rana DP (2017) Review of random forest classification techniques to resolve data imbalance. In: 2017 1st International Conference on Intelligent Systems and Information Management (ICISIM). Aurangabad, India. IEEE 72–78. https://doi.org/10.1109/ICISIM.2017.8122151

Morford SL, Allred BW, Jensen ER, Maestas JD, Mueller KR, Pacholski CL, Smith JT, Tack JD, Tackett KN, Naugle DE (2024) Mapping tree cover expansion in Montana, USA rangelands using high-resolution historical aerial imagery. Remote Sens Ecol Conserv 10(1):91–105. https://doi.org/10.1002/rse2.357

Nguyen TA, Kellenberger B, Tuia D (2022) Mapping forest in the Swiss Alps treeline ecotone with explainable deep learning. Remote Sens Environ 281:113217. https://doi.org/10.1016/j.rse.2022.113217

Nguyen TA, Rußwurm M, Lenczner G, Tuia D (2024) Multi-temporal forest monitoring in the Swiss Alps with knowledge-guided deep learning. Remote Sens Environ 305:114109. https://doi.org/10.1016/j.rse.2024.114109

Nita MD, Munteanu C, Gutman G, Abrudan IV, Radeloff VC (2018) Widespread forest cutting in the aftermath of World War II captured by broad-scale historical *Corona* spy satellite photography. Remote Sens Environ 204:322–332. https://doi.org/10.1016/j.rse.2017.10.021

Oliver CD, Larson CB (1996) Forest stand dynamics: updated edition. Environmental Science. John Wiley and sons.

Patino JE, Duque JC (2013) A review of regional science applications of satellite remote sensing in urban settings. Comput Environ Urban Syst 37:1–17. https://doi.org/10.1016/j.compenvurbsys.2012.06.003

Pinto AT, Gonçalves JA, Beja P, Pradinho Honrado J (2019) From archived historical aerial imagery to informative orthophotos: a framework for retrieving the past in long-term socioecological research. Remote Sens 11(11):1388. https://doi.org/10.3390/rs11111388

Pons A, Rullan O (2014a) Artificialization and islandness on the Spanish tourist coast. Misc Geogr Reg Stud Dev 18(1):5–16. https://doi.org/10.2478/mgrsd-2014-0010

Pons A, Rullan O (2014b) The expansion of urbanisation in the balearic islands (1956–2006). J Mar Isl Cult 3(2):78–88. https://doi.org/10.1016/j.imic.2014.11.004

Probst P, Wright MN, Boulesteix AL (2019) Hyperparameters and tuning strategies for random forest. Wiley Interdiscip Rev Data Min Knowl Discov 9(3):e1301. https://doi.org/10.1002/widm.1301

QGIS Development Team (2022) QGIS geographic information system. QGIS Association. https://www.qgis.org

Ramón-Cardona J, Serra-Cantallops A (2014) Historia del turismo en Ibiza: aplicación del ciclo de Vida del destino turístico en un destino maduro del mediterráneo. PASOS Rev De Turismo Y Patrimonio Cult 12(4): 899–913. https://doi.org/10.25145/j.pasos.2014.12.06

Reyes-Palomeque G, Dupuy JM, Portillo-Quintero CA, Andrade JL, Tun-Dzul FJ, Hernández-Stefanoni JL (2021) Mapping forest age and characterizing vegetation structure and species composition in tropical dry forests. Ecol Indic 120:106955. https://doi.org/10.1016/j.ecolind.2020.106955

Ribas-Costa VA, Cook RL, Gastón A (2024) Modeling structural traits of Aleppo pine (*Pinus halepensis* Mill) forests with low-density LiDAR. Eur J Remote Sens 57(1):2344569. https://doi.org/10.1080/22797254.2024.2344569

Del Río M, Calama R, Montero G (2008) Selvicultura de *Pinus halepensis* Mill. in "Compendio de Selvicultura Aplicada en España", Serrada R, Montero G, Reque JA (Eds.) Madrid: Instituto Nacional de investigación y Tecnología Agraria y Alimentaria. Madrid, Spain.

Roig-Coll S, Kechaiga A (2022) A land of extremes: the dance between intensive farming and farmland abandonment. In: "Resources, Strategis and Potentialities for Food System Sustainability in the Mediterranean Area. Bertoret N, Bertoret E (Eds). Ajuntament de València, CEMAS. València, Spain.

Rojas-Briales E. Delgado-Artés R, Cabrera-Bonet M (2018) Human desertification and disempowerment of rural territories. Forestry in the Midst of Global Changes. CRC Press 101–134

Różycki S, Karwel AK, Kurczyński Z (2023) German extermination camps on WWII reconnaissance photographs. Orthorectification process for archival aerial images of cultural heritage sites. Remote Sens 15(10):2587. https://doi.org/10.3390/rs15102587

Schumacher J, Hauglin M, Astrup R, Breidenbach J (2020) Mapping forest age using National Forest Inventory, airborne laser scanning, and Sentinel-2 data. For Ecosyst 7:60. https://doi.org/10.1186/s40663-020-00274-9

Sharma A, Liu XW, Yang XJ (2018) Land cover classification from multi-temporal, multi-spectral remotely sensed imagery using patch-based recurrent neural networks. Neural Netw 105:346–355. https://doi.org/10.1016/j.neunet.2018.05.019

Shimizu K, Murakami W, Furuichi T, Estoque RC (2023) Mapping land use/land cover changes and forest disturbances in Vietnam using a landsat temporal segmentation algorithm. Remote Sens 15(3):851. https://doi.org/10.3390/rs15030851

Smith A (2010) Image segmentation scale parameter optimization and land cover classification using the Random Forest algorithm. J Spatial Sci 55(1):69–79. https://doi.org/10.1080/14498596.2010.487851

Sohn JA, Saha S, Bauhus J (2016) Potential of forest thinning to mitigate drought stress: a meta-analysis. For Ecol Manag 380:261–273. https://doi.org/10.1016/j.foreco.2016.07.046

Souza CM Jr, Shimbo JZ, Rosa MR, Parente LL, Alencar AA, Rudorff BFT, Hasenack H, Matsumoto M, Ferreira LG, Souza-Filho PWM, de Oliveira SW, Rocha WF, Fonseca AV, Marques CB, Diniz CG, Costa D, Monteiro D, Rosa ER, Vélez-Martin E, Weber EJ, Lenti FEB, Paternost FF, Pareyn FGC, Siqueira JV, Viera JL, Neto LCF, Saraiva MM, Sales MH, Salgado MPG, Vasconcelos R, Galano S, Mesquita VV, Azevedo T (2020) Reconstructing three decades of land use and land cover changes in Brazilian biomes with landsat archive and earth engine. Remote Sens 12(17):2735. https://doi.org/10.3390/rs12172735

Speer JH (2010) Fundamentals of tree-ring research. University of Arizona Press 368. https://doi.org/10.5860/choice.48-1462

Stehman SV (2014) Estimating area and map accuracy for stratified random sampling when the strata are different from the map classes. Int J Remote Sens 35(13):4923–4939. https://doi.org/10.1080/01431161.2014.930207

Stevenson M, Sergeant E, Firestone S (2023) *epiR*: tools for the analysis of epidemiological data. R package version 2.0.66. https://CRAN.R-project.org/package=epiR

Tadese M, Kumar L, Koech R, Kogo BK (2020) Mapping of land-use/land-cover changes and its dynamics in Awash River Basin using remote sensing and GIS. Remote Sens Appl Soc Environ 19:100352. https://doi.org/10.1016/j.rsase.2020.100352

Tassi A, Vizzari M (2020) Object-oriented LULC classification in google earth engine combining SNIC, GLCM, and machine learning algorithms. Remote Sens 12(22):3776. https://doi.org/10.3390/rs12223776

Thomas VA, Wynne RH, Kauffman J, McCurdy W, Brooks EB, Thomas RQ, Rakestraw J (2021) Mapping thins to identify active forest management in southern pine plantations using Landsat time series stacks. Remote Sens Environ 252:112127. https://doi.org/10.1016/j.rse.2020.112127

Tolan J, Yang HI, Nosarzewski B, Couairon G, Vo HV, Brandt J, Spore J, Majumdar S, Haziza D, Vamaraju J, Moutakanni T, Bojanowski P, Johns T, White B, Tiecke T, Couprie C (2024) Very high resolution canopy height maps from RGB imagery using self-supervised vision transformer and convolutional decoder trained on aerial lidar. Remote Sens Environ 300:113888. https://doi.org/10.1016/j.rse.2023.113888

Van den Broeck WAJ, Goedemé T, Loopmans M (2022) Multiclass land cover mapping from historical orthophotos using domain adaptation and spatio-temporal transfer learning. Remote Sens 14(23):5911. https://doi.org/10.3390/rs14235911

Varo-Martínez MÁ, Navarro-Cerrillo RM, Hernández-Clemente R, Duque-Lazo J (2017) Semi-automated stand delineation in Mediterranean *Pinus sylvestris* plantations through segmentation of LiDAR data: the influence of pulse density. Int J Appl Earth Obs Geoinf 56:54–64. https://doi.org/10.1016/j.jag.2016.12.002

Vastaranta M, Niemi M, Wulder MA, White JC, Nurminen K, Litkey P, Honkavaara E, Holopainen M, Hyyppä J (2016) Forest stand age classification using time series of photogrammetrically derived digital surface models. Scand J Res 31(2):194–205. https://doi.org/10.1080/02827581.2015.1060256

Véga C, St-Onge B (2009) Mapping site index and age by linking a time series of canopy height models with growth curves. For Ecol Manag 257(3):951–959. https://doi.org/10.1016/j.foreco.2008.10.029

Vidal-Macua JJ, Ninyerola M, Zabala A, Domingo-Marimon C, Gonzalez-Guerrero O, Pons X (2018) Environmental and socioeconomic factors of abandonment of rainfed and irrigated crops in northeast Spain. Appl Geogr 90:155–174. https://doi.org/10.1016/j.apgeog.2017.12.005

Wang YJ, Qi QW, Liu Y, Jiang LL, Wang J (2019) Unsupervised segmentation parameter selection using the local spatial statistics for remote sensing image segmentation. Int J Appl Earth Obs Geoinf 81:98–109. https://doi.org/10.1016/j.jag.2019.05.004

Weiss A (2001) Topographic position and landforms analysis. Poster presentation, ESRI User Conference, San Diego, CA

Wężyk P, Hawrylo P, Janus B, Weidenbach M, Szostak M (2018) Forest cover changes in Gorce NP (Poland) using photointerpretation of analogue photographs and *GEOBIA* of orthophotos and nDSM based on image-matching based approach. Eur J Remote Sens 51(1):501–510. https://doi.org/10.1080/22797254.2018.1455158

Wright MN, Ziegler A (2017) ranger: a fast implementation of random forests for high dimensional data in *C++* and *R*. J Stat Soft 77(1):1–17

Wulder MA, Franklin SE, White JC, Linke JL, Magnussen S (2006) An accuracy assessment framework for large-area land cover classification products derived from medium——resolution satellite data. Int J Remote Sens 27(4):663–683. https://doi.org/10.1080/01431160500185284

Wulder MA, White JC, Loveland TR, Woodcock CE, Belward AS, Cohen WB, Fosnight EA, Shaw J, Masek JG, Roy DP (2016) The global Landsat archive: status, consolidation, and direction. Remote Sens Environ 185:271–283. https://doi.org/10.1016/j.rse.2015.11.032

Yang XG, Liu YQ, Wu ZC, Yu Y, Li FR, Fan WY (2020) Forest age mapping based on multiple-resource remote sensing data. Environ Monit Assess 192(11):734. https://doi.org/10.1007/s10661-020-08694-4

Zhang C, Sargent I, Pan X, Li HP, Gardiner A, Hare J, Atkinson PM (2019) Joint deep learning for land cover and land use classification. Remote Sens Environ 221:173–187. https://doi.org/10.1016/j.rse.2018.11.014

Zhou HY, Fu LY, Sharma RP, Lei YC, Guo JP (2021) A hybrid approach of combining random forest with texture analysis and VDVI for desert vegetation mapping based on UAV RGB data. Remote Sens 13(10):1891. https://doi.org/10.3390/rs13101891

Publisher's Note Springer Nature remains neutral with regard to jurisdictional claims in published maps and institutional affiliations.